A B

cea
C.E. SACLAY
DSM

SERVICE DE PHYSIQUE NUCLEAIRE
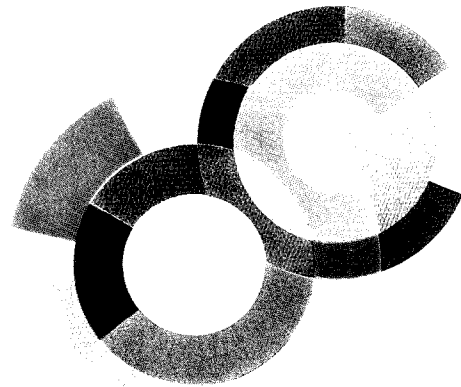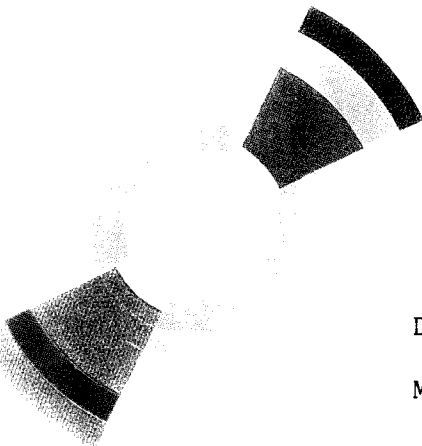
DAPNIA - SPhN 94.01
SW 94 16
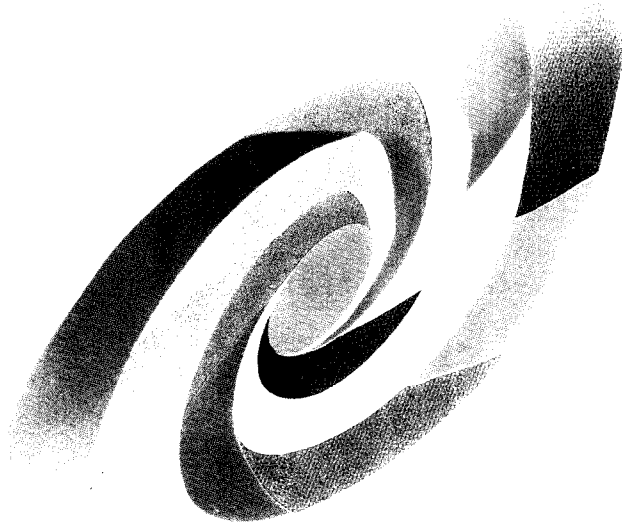
DAPNIA/SPhN 94 01 01/1994

MEASUREMENT OF THE BRANCHING RATIO FOR THE DECAY $\eta \to \mu^+\mu^-$

R. Abegg, A. Baldissieri, A. Boudard,
W. Briscoe, B. Fabbro, M. Garçon,
E.A. Hermes, W.W. Jacobs, R.S. Kessler,
L. Lytkin, B. Mayer, B.M.K. Nefkens,
C. Niebuhr, A.M. Petrov, J. Poitou,
J. Saudinos, B. Tippens, E. Tomasi-
Gustafsson, A. van der Schaaf, W.T.H. van
Oers, S.E. Vigdor, M. Wang, D. White

DAPNIA

Couverture Sylvie Cabrit et Marc Sauvage

Le DAPNIA (**D**épartement d'**A**strophysique, de physique des **P**articules, de physique **N**ucléaire et de l'**I**nstrumentation **A**ssociée) regroupe les activités du Service d'Astrophysique (SAp), du Département de Physique des Particules Elémentaires (DPhPE) et du Département de Physique Nucléaire (DPhN).

Adresse :   DAPNIA, Bâtiment 141
                CEA Saclay
                F - 91191 Gif-sur-Yvette Cedex

Soumis pour publication à :

Physical Review D

MEASUREMENT OF THE BRANCHING RATIO FOR THE DECAY $\eta \to \mu^+\mu^-$

R.Abegg,[1] A.Baldisseri,[2] A.Boudard,[2] W.Briscoe,[3] B.Fabbro,[2]

M.Garçon,[2] E.A.Hermes,[4] W.W.Jacobs,[5,6] R.S.Kessler,[7]

L.Lytkin,[8,6] B.Mayer,[2] B.M.K.Nefkens,[7] C.Niebuhr,[4]

A.M.Petrov,[3] J.Poitou,[2] J.Saudinos,[6] B.Tippens,[7]

E.Tomasi-Gustafsson,[2] A. van der Schaaf,[4] W.T.H. van Oers,[1,6]

S.E.Vigdor,[5,6] M.Wang,[7] and D.White.[7]

January 21, 1994

0

[1] TRIUMF, 4004 Wesbrook Mall, Vancouver, B.C., V6T 2A3 Canada

[2] Service de Physique Nucléaire, Centre d'Etudes de Saclay,

F-91191 Gif-sur-Yvette, France

[3] Center for Nuclear Studies and Department of Physics,

The George Washington University, Washington D.C., 20052, USA

[4] Physik-Institut der Universität Zürich, CH-8057 Zürich, Switzerland

[5] Indiana University Cyclotron Facility,

2401 Milo B. Sampson Lane, Bloomington, Indiana, 47408, USA

[6] Laboratoire National Saturne, F-91191 Gif-sur-Yvette, France

[7] Department of Physics, University of California,

Los Angeles, California, 90024, USA

[8] Joint Institute for Nuclear Research, Dubna, RU-141980 Russia

ABSTRACT

A new measurement of the branching ratio for the decay $\eta \to \mu^+\mu^-$, made at the SATURNE II proton synchrotron, resulted in $\Gamma(\eta \to \mu^+\mu^-)/\Gamma(\eta \to all) = [5.7 \pm 0.7 \text{ (stat.)} \pm 0.5 \text{ (syst.)}] \times 10^{-6}$. The reaction $pd \to {}^3He\eta$ close to threshold yielded 800 s^{-1} tagged η's in a narrow momentum band around 257 MeV/c. Muon pairs were detected in two range telescopes. The data obtained consist of 114 events $\eta \to \mu^+\mu^-$ on a background of 14 events. The new value for the branching ratio is 1.3 ± 0.2 times the unitarity lower limit, consistent with most quark and Vector Meson Dominance models which describe the decay as an electromagnetic transition with a two-photon intermediate state. The result resolves the discrepancy between the two previous measurements of this branching ratio.

PACS: 13.20.Jf

1 Introduction

The decay $\eta \to \mu^+ \mu^-$ is an example of a transition between a pseudoscalar meson and a pair of charged leptons, $P^0 \to \ell^+ \ell^-$. Within the framework of the standard model, this process is dominated by a two-photon intermediate state, Fig. 1a. The contribution from the weak interaction, involving the Z^0 as propagator (Fig. 1b), modifies the transition amplitude by less than $\approx 1\%$ [1] and can therefore be safely ignored. The low probability of a fourth order electromagnetic transition makes these decays sensitive to hypothetical interactions that arise from physics beyond the standard model, such as the existence of leptoquark bosons carrying both quark and lepton flavors, Fig. 1c.

It is convenient to consider separately the real and imaginary parts of the electromagnetic contribution to the transition amplitude for $P^0 \to \ell^+ \ell^-$. The imaginary part, which describes *on-shell* intermediate photons, can be related unambiguously to the known amplitude of the decay $P^0 \to \gamma\gamma$ by the unitarity requirement. The resulting model-independent lower limit on the decay width is [2 − 4]

$$ \Gamma(P^0 \to \ell^+ \ell^-) \geq \frac{\alpha^2}{2\beta} \left[\left(\frac{m_\ell}{m_P} \right) \ln \left(\frac{1+\beta}{1-\beta} \right) \right]^2 \times \Gamma(P^0 \to \gamma\gamma) , \qquad (1) $$

where α is the fine structure constant and $\beta = (1 - (2m_\ell/m_P)^2)^{1/2}$ is the velocity of the leptons in the rest frame of the decaying meson. The real part of the transition amplitude depends on the structure of the meson, which is usually described by the $P^0\gamma\gamma$-vertex form factor. Calculations based on quark models, or on the hypothesis of Vector Meson Dominance, give values for $\Gamma(\eta \to \mu^+ \mu^-)$ which are typically 30% larger than the unitarity lower limit [5]. The relations

3

between the real parts of the $\eta \rightarrow \mu^+\mu^-$, $\eta \rightarrow e^+e^-$ and $\pi^0 \rightarrow e^+e^-$ amplitudes are discussed in Sec. 6.2. In the decays $K_L \rightarrow \ell^+\ell^-$ and $K_L \rightarrow \gamma\gamma$ an important contribution has been attributed to the η pole, so similar relations are predicted between $\eta \rightarrow \mu^+\mu^-$ and $K_L \rightarrow \mu^+\mu^-$ [6].

The limits given by Eq. (1) for the branching ratios (BR) of some $P^0 \rightarrow \ell^+\ell^-$ decays are shown in Table 1, together with the measured branching ratios. Note that the unitarity bounds for $P^0 \rightarrow e^+e^-$ are much smaller than those for $P^0 \rightarrow \mu^+\mu^-$. Besides $\eta \rightarrow \mu^+\mu^-$ the only $P^0 \rightarrow \ell^+\ell^-$ decays which have been observed experimentally to date are $\pi^0 \rightarrow e^+e^-$ [7, 8] and $K_L \rightarrow \mu^+\mu^-$ [13 – 15]. In these cases the measured branching ratios are consistent with the expectations for the electromagnetic contribution.

The available measurements of $P^0 \rightarrow \ell^+\ell^-$ severely constrain the masses and couplings of the various types of leptoquarks [16]. Values for the ratio of mass to coupling constant below several hundred GeV/c^2 can be excluded for transitions within the first generation. For transitions between different generations the excluded region reaches up to 200 TeV/c^2 based on the upper limit for BR($K_L \rightarrow e^+e^-$) given in Table 1.

The earliest search for $\eta \rightarrow \mu^+\mu^-$, carried out in 1968 at Brookhaven National Laboratory [17], resulted in BR($\eta \rightarrow \mu^+\mu^-$)$< 20 \times 10^{-6}$ (90% C.L.). A year later the decay was discovered at CERN [18]; based on 18 events, a branching ratio of $(23\pm9)\times10^{-6}$ was obtained, which lies two standard deviations above the prediction. The most recent measurement, made in Serpukhov, yielded 27 ± 8 events on a large background from $\rho \rightarrow \mu^+\mu^-$. The result BR($\eta \rightarrow \mu^+\mu^-$)$= (6.5\pm2.1)\times10^{-6}$ [10] agrees with the expectations for an electromagnetic

transition. The normalization of the CERN experiment was based on a calculated value of $\sigma(\pi^- p \to \eta X)$, which introduced a substantial systematic uncertainty. The Serpukhov measurement was normalized on the Dalitz decay $\eta \to \mu^+ \mu^- \gamma$, which was recorded simultaneously with the $\eta \to \mu^+ \mu^-$ data.

The discovery at the Laboratoire National Saturne (LNS) of a copious source of η's using the reaction pd$\to^3$Heη near threshold [19] led to the construction of a facility dedicated to experiments on η decay. The momentum vector of each η is reconstructed by momentum analysis of the associated ^{3}He in a magnetic spectrometer. The resulting sample has less than 10% background. The η tag avoids the indirect normalization methods based on an η production cross section or on the branching ratio of another η decay which previously led to large systematic uncertainties. A disadvantage of this method of η production is the high rate in the detection system caused by beam interactions in the deuterium target.

The measurement of BR($\eta \to \mu^+ \mu^-$) described here is the first decay experiment performed at the new facility. Earlier accounts of this experiment can be found in [20] and [21]. The article is organized as follows. The detection procedures are discussed in Sec. 2, which includes detailed descriptions of the beam properties, the kinematics of η production and decay, the η tagging facility, the muon detectors, the trigger logic and the data acquisition. In Sec. 3 the event simulation is described, while Sec. 4 deals with the procedures of the event reconstruction and selection. The evaluation of BR($\eta \to \mu^+ \mu^-$) is presented in Sec. 5 and the result is discussed in Sec. 6.

5

2 Experimental Arrangement

In an earlier LNS experiment [22] the pd→^{3}Heη cross section has been measured at different values for the proton energy above threshold,

$$\Delta T_p \equiv T_p - T_p^0 \ , \tag{2}$$

where T_p is the proton kinetic energy and T_p^0 is its value at threshold; T_p^0=891.4 MeV based on a recent measurement of the η mass [23]. These studies reveal that the cross section rises from threshold to a value of 0.4 μb at ΔT_p=2 MeV, above which it remains approximately constant up to at least ΔT_p=10 MeV. To maximize the product of pd→^{3}Heη cross section and $\eta \rightarrow \mu^+\mu^-$ acceptance, the beam was tuned to ΔT_p=1.6 MeV, where the cross section amounts to about 90% of the value in the plateau. The energy spread of the beam was 0.5 MeV (FWHM) and the average energy loss in the 6.5 mm thick liquid deuterium target was 0.3 MeV.

The kinematics of pd→^{3}Heη at ΔT_p=1.6 MeV, followed by the decay $\eta \rightarrow \mu^+\mu^-$, are illustrated in Fig. 2. At this beam energy, the ^{3}He momentum band is 1320 $\pm$ 30 MeV/c and the maximum laboratory emission angles are 1.2° for the ^{3}He and 6° for the η. These narrow distributions resulted in a 100% geometric acceptance for the ^{3}He spectrometer. For $\eta \rightarrow \mu^+\mu^-$ decays which are symmetric with respect to the η direction, each muon is emitted with a kinetic energy around 200 MeV at an angle of 63°. Because of the small spread in η momentum, the variation in kinetic energy of the muons at a given lab angle in the region around 63° is only about $\pm$15 MeV. The corresponding narrow range distribution facilitated the design of efficient muon detectors located symmetrically

about the target.

2.1 The η Tagging Facility

The recoil ^{3}He particles were detected by the magnetic spectrometer SPES II, which consists of a quadrupole magnet Q and two horizontal dipole magnets D1 and D2, see Fig. 3. The magnetic rigidity (p/Z) of the incident protons was 2.4 times that of the recoil ^{3}He and consequently the proton beam could exit through a window between D1 and D2. Vacuum was maintained between the liquid deuterium target and the exit window of D2 to reduce multiple scattering of the ^{3}He particles along the 8 m flight path. The detection system of SPES II consisted of three multi-wire proportional chambers, followed by scintillator planes A and B. Each wire chamber contained two planes of 256 sense wires, oriented at $\pm 45^0$ with respect to the vertical. The acceptance was defined by an array of six $10 \times 10 \times 0.5$ cm^3 scintillator elements, A1-A6, which spanned a $\pm 10\%$ momentum band. The B-plane was defined by a 100 cm wide by 22.6 cm high and 1.0 cm thick scintillator, positioned 157 cm behind the A counters. This detector was viewed by a photomultiplier at each end to reduce the position dependence of the light collection. The mean time-of-flight (TOF) for the ^{3}He particles between the A and B planes was 12 ns. The TOF resolution was ≈ 1 ns (FWHM).

Eta tagging was accomplished by two independent means: (i) ^{3}He identification using the pulse height in the A hodoscope and the TOF between A and B (see Fig. 4a), and (ii) kinematic selection of pd$\rightarrow$^{3}Heη (see Table 2) using the ^{3}He momentum dispersion, δ_{He} (see Fig. 4b), and emission angles, θ_{He}^h and

7

θ^v_{He}, obtained from the reconstructed trajectory through SPES II. The selection efficiency for pd→^{3}Heη events was 94%. Half of the losses were due to track ambiguities resulting from multiple hits in the wire planes; the remaining losses were due to the constraints of Table 2. The background observed in the sample of tagged η's was investigated by lowering the beam energy by 2.5 MeV, which brings it below the threshold for η production. The resulting δ_{He} distribution was consistent with the fit of the background shown in Fig. 4b. Roughly half of the 8% background originated in beam interactions in the 15 μm titanium windows of the LD$_2$ target; most of the remainder came from the reactions pd→^{3}He$\pi^+\pi^-$ and pd→^{3}He$\pi^0\pi^0$.

Variations of the mean value of ΔT_p between 1.3 and 1.9 MeV during the three-week long experiment had to be taken into account in the evaluation of the $\eta \rightarrow \mu^+\mu^-$ acceptance. These drifts were determined to within ± 0.1 MeV by monitoring the total width of the δ_{He} distribution; $\Delta T_p \simeq (26 \times \delta^{total}_{He})^2$ MeV. The beam intensity was monitored with two plastic scintillator telescopes, which detected charged particles emerging at $\pm 42^0$ lab angle from an 8 μm mylar foil located in the beam 1 m upstream of the LD$_2$ target. For an average intensity of 10^{11} protons per spill of 0.7 s duration, every 1.5 s, the η rate was 800 s^{-1}. The number of tagged η's accumulated during the $\eta \rightarrow \mu^+\mu^-$ data taking period was determined from the number of events in the δ_{He} peak to be

$$N(pd \rightarrow^3 He\eta) = (1.22 \pm 0.01) \times 10^9 .$$
(3)

8

2.2 The Muon Detectors

Two muon detectors, positioned at angles of $\pm 63^0$, were used to determine emission angle, flight time, energy deposition and range of the η decay products. Each detector consisted of a horizontal and a vertical position hodoscope P, followed by trigger hodoscopes T and six planes of stop counters S (see Fig. 5). A wedge-shaped iron degrader W was placed in front of each detector to reduce the rates in the P counters. The thickness of this degrader was 3.0 cm at its center. The wedge slope was 11°, chosen to minimize the variation in energy of the emerging muons across the detector.

The acceptance of the detectors was defined largely by the front P hodoscopes, which had a height of 31.5 cm and a width of 25.8 cm, located 60 cm from the target. Each horizontal and vertical position hodoscope consisted of two planes of eight 1.0 cm thick scintillator strips. The strips in each plane were spaced at distances of one third strip width and the resulting gaps were filled with lucite, to give a smooth energy-loss distribution across the surface of the hodoscope. By offsetting the two planes by one third of a strip width, half of the particles crossing the hodoscope gave signals in both planes. This configuration gives a position resolution which is two times better than would have been obtained with a contiguous array of 16 identical scintillator strips covering the same area. The instantaneous rates were a few times 10^5 s^{-1} in each of the 64 elements of P.

A 5.3 cm thick degrader D was placed between the P and T hodoscopes, so that muons from $\eta \rightarrow \mu^+\mu^-$ came to rest in one of the S counters. This second degrader was made of lead for optimal attenuation of electromagnetic showers, in particular from the decay $\eta \rightarrow \gamma\gamma$. The arrangement of the T ho-

9

doscopes was identical to that of the P hodoscopes, except that fewer scintillators were used. Each of the six S planes consisted of two $71.0 \times 28.0 \times 5.08$ cm^3 blocks of plastic scintillator viewed by phototubes of diameter 12.5 cm placed at one end. Typical singles rates in the T and S counters were a few times 10^5 s^{-1} and 10^6 s^{-1}, respectively.

The angular resolution of each muon detector was 20 mrad (FWHM) both vertically and horizontally; this value includes the broadening due to multiple scattering in W. The range straggling was $\approx$ 7 cm (FWHM) of scintillator material, corresponding to a muon energy resolution of 12 MeV. Further details on the muon detectors are given in [20].

2.3 Trigger Electronics and Data Acquisition

The trigger logic was organized to select three different data streams: (i) the ^{3}He data stream, a known fraction of the events triggering the A-plane of the SPES II spectrometer, used to determine the total number of η's produced; (ii) the $\eta \rightarrow \mu^+\mu^-$ data stream, triple coincidences between the A-plane and the two muon detectors, containing the $\eta \rightarrow \mu^+\mu^-$ candidates; (iii) the pulser data stream, triple coincidences generated electronically, used to determine dead-time effects on the trigger efficiency and losses in the event reconstruction caused by pile-up of the detector signals. Since the ^{3}He and $\eta \rightarrow \mu^+\mu^-$ data streams were recorded simultaneously, the measured value of BR($\eta \rightarrow \mu^+\mu^-$) is independent of uncertainties in the beam intensity, the target thickness, the ^{3}He tagging efficiency and the computer dead-time. The pulser rate was varied proportionally to the rate in the beam monitors and was adjusted to give 2-3 events per cycle. In this

10

way the pulser events had the same time distribution during the beam spill as the $\eta \rightarrow \mu^+\mu^-$ events. The pulse generator sent signals to LED's at one of the A counters and a few elements of the muon detectors. In the case of the P counters, which were not equipped with LED's, the pulser signals were introduced at the inputs of some of the discriminators.

A diagram of the trigger logic is shown in Fig. 6. The A-plane trigger was given by the OR of the discriminator signals of the six A counters. The A rate was limited to $\approx 10^4$ s^{-1} by the use of high discriminator thresholds which were set to reject pions, protons and most of the deuterons, see Fig. 4a. The fraction of the A-plane triggers selected in the ^{3}He data stream was chosen to give roughly one event per beam spill.

The position hodoscopes, which gave the best time resolution, were used redundantly in the trigger by defining both left–right coincidences, $P_L \cdot P_R$, and coincidences with the trigger hodoscope on each side, $L \equiv P_L \cdot T_L$ and $R \equiv P_R \cdot T_R$. With an on-line resolution of ≈ 2.5 ns (FWHM) for the time difference between the two muon detectors, the 10 ns wide overlap in the $P_L \cdot P_R$ coincidence accepted an ample sample of accidental coincidences to be studied off-line. The relative timing in the $A \cdot L \cdot R$ coincidence was adjusted to select a 30 ns window on the TOF through SPES II, centered around the pd$\rightarrow^3$Heη peak. The width of the ADC gate was 20 ns for the P counters and 60 ns for the T and S counters.

The P and T hodoscopes recorded $(3-4)\times 10^6$ counts per beam burst each 1.5 s. The corresponding number of counts per muon detector, L and R in Fig. 6, was 6×10^5. The L·R coincidence rate was 3×10^4 per beam burst,

resulting in a trigger rate of $20 - 25$ A·L·R triple coincidences per burst. The event information was read from CAMAC registers by a SAR computer [24]. The events which had valid TDC values for the B counter in the SPES II detection system ($\approx 50\%$ of the events) were stored and copied to tape in between beam bursts. The dead-time introduced by the data acquisition program was about 3%.

The pulser data stream provided a sample of random signals under actual operating conditions. These events were directly incorporated in the event simulation described in the next section. Another purpose of the pulser events was to monitor the trigger efficiency for triple coincidences, $\epsilon_{triple}^{trigger}$, which was assumed to be the same for both event types, giving

$$\epsilon_{triple}^{trigger} = 0.92 \pm 0.03 \ . \tag{4}$$

3 Simulation of the Experiment

A detailed simulation of the experiment was needed to determine the acceptance and the reconstruction efficiency for $\eta \to \mu^+\mu^-$ events. The simulation took into account the phase-space distribution of the incident proton beam and the interactions of the protons, the ^{3}He particles, and the $\mu^+\mu^-$ pairs in the LD$_2$ target. The ^{3}He trajectory was treated using a first-order transport matrix for SPES II. The interactions of the muons in the detectors were simulated with the code GEANT [25], version 3.13.

Table 3 shows the values of the $\eta \to \mu^+\mu^-$ acceptance under various conditions, as deduced from the event simulation. The fraction of events accepted by the hardware trigger is given in the second row. The 16% reduction from the value in the first row is explained by range straggling and multiple scattering in degrader D. Correcting for the deviations of ΔT_p from the value 1.5 MeV assumed in Table 3 results in a value for the acceptance, averaged over the total measuring period, of

$$\mathcal{A}_{\eta \to \mu^+\mu^-} = (2.91 \pm 0.04^{\text{stat}} \pm 0.03^{\text{syst}}) \times 10^{-2} . \tag{5}$$

The systematic error is mainly due to the ± 0.1 MeV uncertainty in the mean value of ΔT_p. Systematic uncertainties associated with the detector geometry affect both the acceptance and the analysis efficiency, and have been included in the uncertainty of the overall $\eta \to \mu^+\mu^-$ selection efficiency, $\epsilon_{\mu^+\mu^-}^{\text{analysis}}$, discussed in Sec. 4.2 and 5.2.

The last two rows of Table 3 reveal that in roughly 20% of the $\eta \to \mu^+\mu^-$ events in which both muons reached the first S plane, at least one of them

13

scattered out of the detector. This event type was accepted by the trigger but could not be recognized unambiguously in the off-line event selection. Since muon identification and range determination were less reliable for these events, their reconstruction efficiency was reduced.

Simulated events which fulfilled the conditions of the hardware trigger were stored in the same data format as the measured events. Time resolutions were adjusted to the observed values. As a consequence of the high singles rates, many events suffered from corrupted TDC values, ambiguous topologies, or pulse height pile-up, which resulted in a 15% reduction in the $\eta \rightarrow \mu^+\mu^-$ reconstruction efficiency. An accurate account of these effects was achieved by directly incorporating the random background observed in the pulser events.

4 Event Reconstruction and Selection

In the first stage of the event reconstruction, the SPES II information was analyzed as described in Sec. 2.1. This part of the data analysis was common to all measured and simulated event types. Roughly half of the recorded triple coincidences satisfied the pd$\rightarrow^3$Heη selection criteria.

A calibration of the pulse heights and the relative timings of all counters in a muon detector was possible throughout the experiment, using energetic charged particles from the sample of triple coincidences. The particles that reached the last S plane were mainly pions, and their pulse height distributions were very similar to those expected for muons from $\eta \rightarrow \mu^+\mu^-$. The relative timing between the two muon detectors and the SPES II spectrometer was calibrated using the decays $\eta \rightarrow \gamma\gamma$ and $\eta \rightarrow 3\pi^0 \rightarrow 6\gamma$. About 65% of the electromagnetic showers produced in the front degraders by photons from these decays resulted in signals in the P hodoscopes. Only a very small fraction of these showers reached into the region of the T counters, but there was a 1% probability for simultaneous random T signals in both detectors, which gave rise to a few hundred triggers per hour associated with prompt triple coincidences.

4.1 Reconstruction of Triple Coincidence Events

Triple coincidence events were reconstructed and characterized in terms of time differences, emission angles, ranges, energy depositions and some particle identification observables, as discussed below.

The scintillator timings were corrected for the dependence on signal

15

amplitude and impact position. In one third of the events of interest, either one of the hit P counters had a TDC value corrupted by a stop signal from a preceding hit, or additional random P hits had occurred. The ADC gates were timed by the triple coincidence signal, which had very little dead time. Most events with TDC losses could thus be recovered by taking into account the pulse-height information. Multiple-hit ambiguities were reduced by rejecting P hits corresponding to large deviations from coplanarity and expected opening angle, as discussed below. Five percent of the events of interest were lost because the muon trajectories could not be reconstructed unambiguously. For the surviving events, an arrival time was calculated for each muon detector as the mean TDC value from the hit P counters, weighted by pulse height and corrected for TOF from the target.

The ^{3}He TOF between the target and the A-plane was corrected for its dependence on the ^{3}He momentum and emission angle, as calibrated with the $\eta \rightarrow \gamma\gamma$ events. Figure 7 shows distributions of the time differences Δt_{LR}, between the two muon detectors, and Δt_{LA}, between the left detector and the A-plane. Both spectra show a pronounced peak with a FWHM of ≈ 0.7 ns. The position of the peak in the Δt_{LA} distribution indicates that most triple coincidence events involve decay products with $v \approx c$, as expected for the $\eta \rightarrow \gamma\gamma$ and $\eta \rightarrow 3\pi^0$ events.

Angle information was deduced from the P hodoscope pattern under the assumption that each trajectory originated in the center of the 6.5 mm thick LD$_2$ target. Since the η momentum vector is known from the analysis of the associated ^{3}He, there are two constraints on the $\mu^+\mu^-$ emission angles in the decay $\eta \rightarrow \mu^+\mu^-$. A first constraint was a test of the coplanarity of the three

momentum vectors. This test was of limited use since it does not discriminate against $\eta \rightarrow \gamma\gamma$ events, and because the angular resolution of SPES II in the vertical plane is relatively poor (see Table 2). The second test was made on $\Delta\theta_{LR}$, defined as the difference between the measured $\mu^+\mu^-$ opening angle, $\theta_{LR}^{measured}$, and its calculated value, θ_{LR}^{calc}, as deduced from the η momentum vector and the mean of the emission angles of the two decay products:

$$\Delta\theta_{LR} \equiv \theta_{LR}^{calc} - \theta_{LR}^{measured} . \tag{6}$$

The detector geometry restricts this opening angle deviation to $|\Delta\theta_{LR}| < 28°$. This range was reduced to $|\Delta\theta_{LR}| < 9°$ in the P hodoscope analysis to help resolve ambiguities. For $\eta \rightarrow \mu^+\mu^-$ decays, the distribution is centered at zero and has a Gaussian shape with a width of $\approx 3.0°$ (FWHM). Since this distribution uniquely identifies the events of interest, it played a central role in the optimization of the various selection criteria.

In each muon detector the range of the muon candidate, R_{meas}, was determined from the last S plane with a prompt TDC value, with a correction for the penetration depth in this plane as deduced from the energy deposition. All S planes preceding the last hit plane were required to have energy loss signals above 6 MeV and time signals in or before the prompt window. Random hits were therefore accepted, except for early signals in the last hit plane. No upper threshold on the pulse height was applied, which avoided losses due to pile-up. A muon range likelihood, W, was calculated, defined as the probability to observe R_{meas} given the most likely value, R_{calc}, calculated from the muon angles and the ^{3}He momentum assuming $\eta \rightarrow \mu^+\mu^-$ kinematics. To good approximation, W depends on the difference $\Delta R \equiv R_{meas} - R_{calc}$ only. The shape of the $W(\Delta R)$

17

distribution has been parametrized using the results from a simulation of muon trajectories through the center of the detector. Normalizing the maximum value to 1, the result is

$$W(\triangle R) \equiv exp\left[-\frac{\triangle R^2}{2\sigma_R^2}\left(1 + 0.0733\triangle R + 0.0022\triangle R^2\right)\right], \qquad (7)$$

with R in cm. The value $\sigma_R \simeq 3.0$ cm is determined mainly by range straggling, which depends slightly on the muon energy. The combined range likelihood, W_{LR}, was the product of the $W(\triangle R)$ values for the two muon detectors. In the approximation of Gaussian $W(\triangle R)$ distributions, W_{LR} has a distribution which is constant in the interval (0,1). Consequently, $\eta \rightarrow \mu^+\mu^-$ events are expected to have an approximately uniform distribution, with a small enhancement at low W_{LR} due to the skewness of the $\triangle R$ distribution given in Eq.(7). An additional contribution to this enhancement arises from out-scattering of muons, an effect ignored in the simulations on which Eq.(7) was based.

The muon identification made use of the characteristic range-energy relation and the observed pattern of stop counter multiplicities. Multiplicities were defined for each plane as the number of counters (0, 1 or 2) with TDC values within the prompt peak and with a pulse height above 6 MeV. Ideally the multiplicity is equal to 1 for the S planes traversed by the muon, and 0 for the remaining planes, but these values may be different due to random hits (few % probability) or detector crossings within one plane ($\approx$0.5 % probability). The likelihood for the occurrence of the measured multiplicity has been calculated for each plane, taking into account the value of R_{calc} and the background multiplicities as measured with pulser events. The total likelihood, L_S, for the observed pattern of S counter multiplicities was defined as the product of the likelihood over the

18

twelve planes. Normalizing the maximum value of L_S to 1, the mean value of L_S for $\eta \to \mu^+\mu^-$ decays, as deduced from the event simulation, was 0.15.

4.2 Selection of $\eta \to \mu^+\mu^-$ Candidates

The selection of $\eta \to \mu^+\mu^-$ candidates proceeded in two stages. First, the number of triple coincidences was reduced by a series of tests on the reconstructed variables. In the second stage the remaining sample of 572 events was analyzed with the help of an event classifier, which was optimized empirically to separate $\eta \to \mu^+\mu^-$ candidates from the background. The distribution of $\Delta\theta_{LR}$, Eq.(6), allows the identification of the dominant event types at each stage of the event selection, see Fig. 8. The corresponding $\eta \to \mu^+\mu^-$ selection efficiencies are given in Table 4. Events were selected which fulfill the ^{3}He requirements, which have timings within the prompt peaks shown in Fig. 7, and which also satisfy the condition $|\Delta\theta_{LR}| < 9^0$. These events show a pronounced peak in $\Delta\theta_{LR}$ (see Fig. 8a), centered at $-4°$, as expected for $\eta \to \gamma\gamma$ events. The underlying flat component is due mainly to $\eta \to 3\pi$. The small bump centered at $+3°$ is from pd$\to^3$He$\pi^+\pi^-$ events associated with the continuum background underneath the pd$\to^3$Heη peak. The third and fourth tests listed in Table 4 reduced these background processes more or less uniformly. The test on the S counter timing was not very restrictive, since it was only asked that one or more stop counters on each detector satisfied the requirement of a ± 5 ns coincidence with respect to the P hodoscope time. The condition $W_{LR} > 0.02$ on the S counter ranges preferentially removed events with electromagnetic showers, such as $\eta \to \gamma\gamma$. In the distribution of the remaining events, shown in Fig. 8c, the $\eta \to \mu^+\mu^-$

19

contribution can be noticed already near $\Delta\theta_{LR}=0°$.

The miscellaneous tests mentioned in Table 4 were (i) a 1.3 MeV lower threshold on the energy depositions in the 1.0 cm thick P counters, (ii) a window on the mean TDC value of all prompt S counters, (iii) a window on the difference between the timing of the A-plane and the mean timing of the two muon detectors, $|\Delta t_{A-LR} - 0.2 \text{ ns}| < 0.7$ ns, where the offset accounts for the additional TOF of the muons as compared to the photons assumed in the timing analysis (iv) a window of $60 - 130$ MeV on the sum of the energies deposited in all S counters on both sides and, finally, (v) a threshold ($\log L_S > -4$) on the S counter multiplicity likelihood. After these requirements the sample contained 572 triple coincidences with roughly equal contributions from $\eta \rightarrow \mu^+\mu^-$ and $\eta \rightarrow \gamma\gamma$, see Fig. 8d. The events with $\Delta\theta_{LR} > 3°$ have a flat time distribution, indicating that the background in the $\Delta\theta_{LR}$ continuum at this stage is dominated by accidental coincidences.

The separation of the $\eta \rightarrow \mu^+\mu^-$ signal from the remaining background was based on their different distributions with respect to various reconstructed variables. Since the background contained many accidental and pile-up events, no attempt was made to simulate these distributions for the background events, as would have been necessary for a proper maximum likelihood analysis. Instead, the distributions *observed* for events inside and outside the region of the $\eta \rightarrow \mu^+\mu^-$ peak in the $\Delta\theta_{LR}$ distribution of Fig. 8d were used empirically to estimate for each candidate in the sample its likelihood to be an $\eta \rightarrow \mu^+\mu^-$ event. This procedure demands that the event classification is independent of $\Delta\theta_{LR}$. Each candidate was described by a vector x, with components x_j, j=1 – 9,

20

constructed from the following variables: (i) left–right time difference, (ii) largest energy deposited in any P hodoscope plane, (iii) remaining energy deposited in the P counters, (iv) energy deposited in the last S plane reached by the muon, (v) total energy in the S counters of both muon detectors, (vi) range-energy relation in the S counters, (vii) average time of all prompt S counters, (viii) average time of all prompt T counters, (ix) deviation from coplanarity of the momentum vectors of the ^{3}He particle and the two muons. In the components (iv) and (vi), the smaller value for the two muon detectors was used, which reduces the influence of pile-up. In general, the likelihood for a candidate to be an $\eta \rightarrow \mu^+\mu^-$ event is given by a complicated function of $\mathbf{x}$ given by the ratio of the probability densities for signal and background in this 9 –dimensional space. Since this function would have to be extracted from the small sample of 572 selected events, a simplified procedure was used to reduce the risk of biasing the result.

For each component x_j the value $\hat{x}_j$ was determined which maximizes the signal to background ratio. The event classifier was approximated by a quadratic expansion around $\hat{x}$:

$$C(\mathbf{x}) \equiv \left[\sum_{j=1}^{9} \alpha_j (x_j - \hat{x}_j)^2 \right]^\beta . \tag{8}$$

The coefficients α_j in Eq.(8) are defined such that $C(\mathbf{x})$ is dimensionless. The values for α_j were obtained iteratively, using events in a region of $C(\mathbf{x})$ where the ratio of signal to background is about one to one. The coefficients α_j were chosen such that each of the nine $C(\mathbf{x})$ components makes a relative contribution which is roughly equal for signal and background events. This procedure results in optimal background suppression. The exact choice of the values of α_j affects the background discrimination, but has no direct systematic effect on the measured

21

value for BR($\eta \rightarrow \mu^+ \mu^-$). The exponent $\beta = 3.55$ was chosen empirically to give a flat $C(\mathbf{x})$ distribution for the background. Figure 9 shows the distribution of $C(\mathbf{x})$ for two $\Delta\theta_{LR}$ intervals. The "signal" distribution, defined by $|\Delta\theta_{LR}| < 3.0°$, shows a pronounced peak at $C(\mathbf{x}) = 0$, which extends to $C(\mathbf{x}) \simeq 20$. The $\Delta\theta_{LR}$ spectra for selected regions in $C(\mathbf{x})$ are shown in Figs. 8e and 8f. The cut on $C(\mathbf{x})$, was varied between 5 and 300, corresponding to efficiencies between 60% and 97% for the simulated $\eta \rightarrow \mu^+ \mu^-$ events passing all other constraints in Table 4. The resulting branching ratio varies within ±4%, which is statistically insignificant. A detailed interpretation of the spectrum in Fig. 8f is given in Sec. 5.1.

Figures 10 and 11 show distributions of two reconstructed observables for $\eta \rightarrow \mu^+ \mu^-$ candidates and for background events. The events were selected using all the cuts described above, *excluding* any information related to the observable in question. The background distributions were taken from the interval $3.5° < |\Delta\theta_{LR}| < 9°$; the $\eta \rightarrow \mu^+ \mu^-$ distributions were obtained from the region $|\Delta\theta_{LR}| < 3°$ and corrected for the continuum background. The simulated spectra are shown as well. Figure 10 shows the distribution of the largest energy deposition in any of the four P planes. This variable was included in the calculation of $C(\mathbf{x})$ to suppress η decays into neutrals since the gamma showers from degrader W often deposited large signals in the P planes. The reliability of the simulation of the range straggling has been checked with the distribution of the range likelihood, W_{LR}, defined above. As is shown in Fig. 11, the measured and simulated distributions agree well, except in the region $W_{LR} < 0.1$ where the simulation seems to underestimate the yield slightly. This possible deviation

22

has been taken into account in the systematic error of the selection efficiency by varying the lower threshold on W_{LR}, as discussed below.

The acceptance of the detection system as defined by the solid angle of the position hodoscope was reduced by 16% due to range straggling and multiple scattering in the degraders (see the first two rows of Table 3). The accuracy of the simulation of these effects has been checked by studying the dependence of the muon range on the η emission angle in the horizontal plane, θ_η^h, shown in Fig. 12. In making these plots the sense of rotation of θ_η^h was chosen to be opposite for the two detectors, in order to give comparable distributions. The magnitude and the angular dependence of the observed mean range are reproduced well by the simulation; this agreement has been used to assess the systematic error in the selection efficiency, introduced by uncertainties in the geometry (see Sec. 5.2).

5 Determination of the Branching Ratio of $\eta \to \mu^+\mu^-$

The branching ratio of $\eta \to \mu^+\mu^-$ was obtained from the expression

$$\text{BR}(\eta \to \mu^+\mu^-) = \frac{N(\eta \to \mu^+\mu^-)}{N(\text{pd} \to {}^3\text{He}\eta)} \left(\mathcal{A}_{\eta \to \mu^+\mu^-} \cdot \epsilon_{\text{triple}}^{\text{trigger}} \cdot \epsilon_{\mu^+\mu^-}^{\text{analysis}} \right)^{-1} , \qquad (9)$$

where $N(\eta \to \mu^+\mu^-)$ is the number of $\eta \to \mu^+\mu^-$ events extracted as described below, $N(\text{pd}\to{}^3\text{He}\eta)$ is the number of tagged η's given by expression (3), $\mathcal{A}_{\eta \to \mu^+\mu^-}$ is the $\eta \to \mu^+\mu^-$ acceptance given by expression (5), $\epsilon_{\text{triple}}^{\text{trigger}}$ is the trigger efficiency given by expression (4) and $\epsilon_{\mu^+\mu^-}^{\text{analysis}}$ is the efficiency of the $\eta \to \mu^+\mu^-$ event selection, to be discussed in Sec. 5.2.

5.1 The Determination of $N(\eta \to \mu^+\mu^-)$

The distribution of $\Delta\theta_{\text{LR}}$ for events with $C(\mathbf{x})< 25$ is shown in Fig. 13, along with the distribution predicted by the simulation of $\eta \to \mu^+\mu^-$. The level of the constant background in the simulation has been adjusted to the measured distribution in the region $|\Delta\theta_{\text{LR}}|> 3.5°$. The agreement between the observed and simulated peak shapes is excellent.

Three other contributions to the distribution in Fig. 13 have been studied. First, the rate for the Dalitz decay $\eta \to \mu^+\mu^-\gamma$ with a soft photon has been calculated using the formalism given in Ref. [26]. A conservative estimate for $E_\gamma < 30$ MeV gives a contribution of less than 0.5 event, which has been ignored.

The second process which has been investigated is $\text{pd}\to{}^3\text{He}\pi^+\pi^-$, followed by the decay of one or both pions, $\pi \to \mu\nu$. As a first step the reaction

pd→^{3}He$\pi^+\pi^-$ was studied in a separate measurement with the front degraders removed, using the P counters only. Upon application of the pd→^{3}Heη phase space cuts listed in Table 2, and after corrections were made for the $\pi^+\pi^-$ acceptance and detection efficiency, the relative yield was found to be

$$\frac{\mathcal{Y}(\text{pd} \rightarrow {}^3\text{He } \pi^+\pi^-)}{\mathcal{Y}(\text{pd} \rightarrow {}^3\text{He } \eta)} = (1.7 \pm 0.3) \times 10^{-2} \ . \tag{10}$$

As a second step a simulation with GEANT was used to estimate the pd→^{3}He$\pi^+\pi^-$ background in the sample of $\eta \rightarrow \mu^+\mu^-$ candidates. These simulated events satisfied the hardware trigger at the level of 7×10^{-7} per η decay. In reality, many more pd→^{3}He$\pi^+\pi^-$ events passed the hardware trigger by means of random signals from the T hodoscopes, but these events were eliminated by the S counter analysis. The simulation indicates a pd→^{3}He$\pi^+\pi^-$ level of 1.3×10^{-8} per η decay in the final sample, mainly from events in which both pions decay before reaching the muon detectors, which corresponds to a contribution of 0.3 background events.

The third source of background studied, is pd→^{3}He$\mu^+\mu^-$ where the ^{3}He was accepted by the criteria of the η tag. In the best previous $\eta \rightarrow \mu^+\mu^-$ experiment [10], this background was 50% larger than the $\eta \rightarrow \mu^+\mu^-$ signal. A possible source of this background is the tail of the ρ resonance ($m_\rho \simeq 770$ MeV, $\Gamma_\rho \simeq 150$ MeV). Since BR($\rho \rightarrow \mu^+\mu^-$)= $(4.6 \pm 0.3) \times 10^{-5}$ is nearly ten times larger than BR($\eta \rightarrow \mu^+\mu^-$), the continuum background of ρ underneath the η peak is enhanced by this factor in the $\mu^+\mu^-$ channel. The pd→^{3}He$\mu^+\mu^-$ background was extrapolated from pd→^{3}HeX events, selected well outside the phase space region for ^{3}He from the reaction pd→^{3}Heη (see Table 2). No likely candidates were found, which resulted in an upper limit of four pd→^{3}He$\mu^+\mu^-$ events (70%

C.L.) contributing to the peak in Fig. 13, i.e., less than 4% of the $\eta \to \mu^+\mu^-$ signal. The number of $\eta \to \mu^+\mu^-$ candidates with $|\Delta\theta_{LR}| < 3°$ in the spectrum of Fig. 13 has been determined under the assumption of a linear background, to be 114 ± 14. The contribution from $pd \to {}^3He\mu^+\mu^-$ was taken into account by subtracting 0^{+4}_{-0} events, resulting in

$$N(\eta \to \mu^+\mu^-) = 114^{+14}_{-15} \tag{11}$$

5.2 Efficiency of the $\eta \to \mu^+\mu^-$ Selection

The overall $\eta \to \mu^+\mu^-$ analysis efficiency, $\epsilon^{analysis}_{\mu^+\mu^-}$, was deduced from the event simulation; the result was presented in Table 4. Due to the strong correlations among the various criteria in the event selection, it is not appropriate to determine the uncertainty in $\epsilon^{analysis}_{\mu^+\mu^-}$ as the quadratic sum of errors in the efficiency factors for the individual tests listed in Table 4. Instead, the error has been determined directly by varying various quantities within their limits.

Changing the ADC values and the TDC offsets in the simulation by 10% and 1 ns, respectively, gave relative variations of $\pm 4\%$ in $\epsilon^{analysis}_{\mu^+\mu^-}$. The selection efficiency is affected by several uncertainties in the detector geometry. Uncertainties in the distribution of detector material along the muon paths were assessed by studying the distribution of the last S plane hit versus θ^h_η, shown in Fig. 12. The measured distribution has a mean value at $\theta^h_\eta = 0$ mrad of 2.77 ± 0.05 (stat.), as compared to 2.74 ± 0.01 (stat.) for the simulated distribution. A systematic uncertainty in the muon range of ± 0.1 S counter units or ± 0.5 g/cm^2 leads to an uncertainty in $\epsilon^{analysis}_{\mu^+\mu^-}$ of $\pm 1\%$. Error contributions from the $\pm 1°$ uncertainty in detector angle and from misalignments by a few millimeters of various detector

26

elements were added in quadrature; the net systematic error in $\epsilon_{\mu^+\mu^-}^{\text{analysis}}$ due to geometric uncertainties is thus $\pm 2\%$.

Multiple scattering in the iron and lead degraders led to a 15% efficiency loss, distributed over various selection criteria. The systematic uncertainty in $\epsilon_{\mu^+\mu^-}^{\text{analysis}}$ associated with the simulation of these losses was determined by replacing the standard GEANT treatment, which uses Molière theory, by a Gaussian approximation which is known to be very poor for large-angle scattering. The corresponding change in $\epsilon_{\mu^+\mu^-}^{\text{analysis}}$ was 6.4% and the conservative estimate assumed for this contribution to the error in $\epsilon_{\mu^+\mu^-}^{\text{analysis}}$ is $\pm 3\%$. This uncertainty includes the effect of multiple scattering losses on the acceptance (see Table 3, rows 1 and 2).

The combined systematic error resulting from the sources discussed above amounts to $\pm 6\%$. This value has been checked by varying the criteria in the event selection. As discussed in Sec. 4.2, the systematic uncertainty in $\epsilon_{\mu^+\mu^-}^{\text{analysis}}$ introduced by the cut on $C(\mathbf{x})$, which is responsible for most of the losses in the event selection, is within $\pm 4\%$. The systematic error due to all selection criteria was evaluated to be $\pm 6\%$, which is equal to the value from the three sources studied explicitly. Conservatively, it was assumed that these two estimates represent independent error sources, which leads to an overall analysis efficiency of

$$\epsilon_{\mu^+\mu^-}^{\text{analysis}} = 0.61 \pm 0.05 . \tag{12}$$

6 Result and Discussion

6.1 The Result for BR($\eta \to \mu^+\mu^-$)

The branching ratio of $\eta \to \mu^+\mu^-$ was calculated using expression (9). The values of the various quantities appearing in this expression are given in Table 5. The result is

$$\mathrm{BR}(\eta \to \mu^+\mu^-) \equiv \frac{\Gamma(\eta \to \mu^+\mu^-)}{\Gamma(\eta \to \mathrm{all})} = [5.7 \pm 0.7(\mathrm{stat.}) \pm 0.5(\mathrm{syst.})] \times 10^{-6} . \quad (13)$$

This new value is compared with previous results in Fig. 14. Adding the statistical and systematic errors in quadrature and normalizing the result to the unitarity bound given in Table 1, one obtains

$$\mathcal{R} \equiv \frac{\mathrm{BR}(\eta \to \mu^+\mu^-)}{\mathrm{BR}_{\mathrm{unit.}}(\eta \to \mu^+\mu^-)} = 1.3 \pm 0.2 . \quad (14)$$

This result is consistent with the previous Serpukhov value of $\mathcal{R} = 1.5 \pm 0.5$ [10], but does not support the earlier CERN value of $\mathcal{R} = 5.3 \pm 2.1$ [18]. The result demonstrates the dominance of the on-shell two-photon intermediate state. Since it agrees with the predictions for the electromagnetic contribution, there is no need to invoke physics beyond the standard model.

6.2 Connection with Other $P^0 \to \ell^+\ell^-$ Decays

It has been noted [27,28] that the various $P^0 \to \ell^+\ell^-$ branching ratios can be interrelated in an almost model-independent way. A reduced amplitude $R(q^2)$ is defined by

$$\frac{\Gamma(P^0 \to \ell^+\ell^-)}{\Gamma(P^0 \to \gamma\gamma)} = 2\beta \left(\frac{\alpha}{\pi}\frac{m_\ell}{m_P}\right)^2 |R(m_P{}^2)|^2 , \quad (15)$$

with the imaginary part of $R(m_P^2)$ predicted by QED:

$$\text{Im}R(m_P^2) = -\frac{\pi}{2\beta}\ln\frac{1+\beta}{1-\beta} \tag{16}$$

Equations (15) and (16) lead to the unitarity bound given in Eq.(1). The present result for BR($\eta \to \mu^+\mu^-$) given by expression (13) leads to

$$|\text{Re}R_{\eta\to\mu\mu}(m_\eta^2)| = 2.8 \pm 1.1 \tag{17}$$

As shown in Ref. [27], most of the model-dependence of the real part of the amplitude cancels in the *difference* in $\text{Re}R(m_P^2)$ for the decays $P^0 \to e^+e^-$ and $P^0 \to \mu^+\mu^-$. For the η decays one obtains

$$\text{Re}R_{\eta\to\mu\mu} - \text{Re}R_{\eta\to ee} = -32 \pm 2 \tag{18}$$

Using the result (17), Eq.(18) leads to the following predictions for the branching ratio of $\eta \to e^+e^-$

$$\text{BR}_{\text{calc.}}(\eta \to e^+e^-) = (6.2 \pm 0.8) \times 10^{-9}, \quad \text{Re}R_{\eta\to\mu\mu} > 0 \tag{19}$$

$$\text{BR}_{\text{calc.}}(\eta \to e^+e^-) = (4.8 \pm 0.7) \times 10^{-9}, \quad \text{Re}R_{\eta\to\mu\mu} < 0. \tag{20}$$

Either prediction is roughly three times the unitarity value, see Table 1; a very similar prediction results from the approach in Ref. [28]. The decay rates observed so far, for $\eta \to \mu^+\mu^-$, $K_L \to \mu^+\mu^-$ and $\pi^0 \to e^+e^-$, are much closer to the unitarity limit. The experimental upper limit for $\text{BR}_{\text{exp}}(\eta \to e^+e^-)$ is 3×10^{-4} (90% C.L.) [9].

The difference in the real parts of the transition amplitudes for the decays $\eta \to \mu^+\mu^-$ and $\pi^0 \to e^+e^-$ is slightly model-dependent. Following Ref. [27] one obtains

$$\text{Re}R_{\pi\to ee} - \text{Re}R_{\eta\to\mu\mu} \simeq 12 + 3\ln\frac{\Lambda_\eta}{\Lambda_\pi}. \tag{21}$$

29

Assuming for the cutoff parameters $\Lambda_\pi < \Lambda_\eta < 2\Lambda_\pi$, the uncertainty in the above prediction is only ± 1, which leads to the following estimates for the branching ratio of $\pi^0 \to e^+ e^-$

$$\mathrm{BR}_{\mathrm{calc.}}(\pi^0 \to e^+ e^-) = (7.9 \pm 0.9) \times 10^{-8}, \quad \mathrm{Re} R_{\eta \to \mu\mu} > 0 \quad (22)$$

$$\mathrm{BR}_{\mathrm{calc.}}(\pi^0 \to e^+ e^-) = (5.9 \pm 0.6) \times 10^{-8}. \quad \mathrm{Re} R_{\eta \to \mu\mu} < 0 \quad (23)$$

Since both predictions agree with the recent experimental results for the branching ratio of $\pi^0 \to e^+ e^-$ [7,8] the sign-ambiguity in the real part of the $\eta \to \mu^+ \mu^-$ amplitude (17) cannot be resolved yet.

6.3 Summary

The measurement of the branching ratio of $\eta \to \mu^+ \mu^-$ is the first decay experiment at the SATURNE η facility. The result is BR($\eta \to \mu^+\mu^-$)= [5.7 $\pm$ 0.7(stat.) $\pm$ 0.5(syst.)] $\times 10^{-6}$. The improvement over earlier results is due to increased statistics (114 events compared to 27 and 18 events for the two previous experiments), a much lower level of background, and elimination of systematic uncertainties associated with the η flux. The largest contribution to the systematic error in the present experiment is introduced by the $\pm 9\%$ uncertainty in the determination of the efficiency of the data reduction off-line.

The new value for the branching ratio is 1.3 ± 0.2 times the unitarity lower limit, consistent with most quark and Vector Meson Dominance models which describe the decay as an electromagnetic transition with a two-photon intermediate state. Consequently, the result leaves little room for a contribution from physics beyond the standard model.

30

TABLES:

Table 1: Values for the branching ratios of some $P^0 \rightarrow \ell^+\ell^-$ modes. Both the experimental results, prior to this experiment, and the unitarity lower bounds are given.

decay mode	$\Gamma(P^0 \rightarrow \ell^+\ell^-) \,/\, \Gamma(P^0 \rightarrow \text{all})$		
	measured value	reference	unitarity bound [a]
$\pi^0 \rightarrow e^+e^-$	$(8.0^{+4.1}_{-2.9} \pm 0.5) \times 10^{-8}$	[7]	4.8×10^{-8}
	$(6.7 \pm 2.0) \times 10^{-8}$	[8]	
$\eta \rightarrow e^+e^-$	$< 3.0 \times 10^{-4}$ (90% C.L.)	[9]	1.8×10^{-9}
$\eta \rightarrow \mu^+\mu^-$	$(6.5 \pm 2.1) \times 10^{-6}$	[10]	4.3×10^{-6}
$K_L \rightarrow e^+e^-$	$< 1.6 \times 10^{-10}$ (90% C.L.)	[11]	3.0×10^{-12}
$K_L \rightarrow \mu^+\mu^-$	$(7.2 \pm 0.4) \times 10^{-9}$	[12]	6.8×10^{-9}

[a]The values for the η decays are based on $\Gamma(\eta \rightarrow \gamma\gamma)=0.39 \times \Gamma(\eta \rightarrow all)$ [12]

Table 2: The SPES II resolution and the software windows used to select pd→^{3}Heη events. The reconstructed quantities were $\delta_{He} \equiv (p_{He} - \langle p_{He} \rangle)/\langle p_{He} \rangle$, and the ^{3}He emission angles in the horizontal and vertical plane, θ_{He}^h and θ_{He}^v, respectively. The quantity $\langle p_{He} \rangle$ is the central value of p_{He} in the reaction pd→^{3}Heη.

observable	resolution (FWHM)	window for pd→^{3}Heη
δ_{He}	0.6%	±3.0%
θ_{He}^h	10 mr	±30 mr
θ_{He}^v	25 mr	±40 mr

Table 3: The fraction of simulated $\eta \to \mu^+\mu^-$ events which pass the various selection criteria at ΔT_p=1.5 MeV. The first two conditions are part of the trigger for data readout. S_L and S_R denote signals in the first S plane of the left and right muon detector, respectively; the other symbols are defined in Fig. 6. Trigger inefficiencies are not included. Errors are statistical only.

selection conditions	acceptance (%)
$P_L \cdot P_R$	3.49 ± 0.04
$L \cdot R$	2.92 ± 0.04
$L \cdot R \cdot S_L \cdot S_R$	2.83 ± 0.04
$L \cdot R \cdot$[both muons stop in S]	2.24 ± 0.03

Table 4: The number of triple coincidence events and the cumulative $\eta \rightarrow$ $\mu^+\mu^-$ efficiency at different stages of the event selection. The efficiency has been deduced from the simulated events before and after random hits have been incorporated and has been normalized to 100% after the η selection, which is common to the triple coincidence and $pd \rightarrow {}^3He\eta$ data streams. The labels in the last column refer to the corresponding $\Delta\theta_{LR}$ distributions in Fig. 8. The uncertainties in the efficiency determination are discussed in Sec. 5.

major additional test	events	cumulative $\eta \rightarrow \mu^+\mu^-$ efficiency		Fig. 8 frame
		random hits		
		yes	no	
none	1.0×10^7			
$pd \rightarrow {}^3He\eta$ selection	5.3×10^6	1.00	1.00	
prompt P counters	1.6×10^5	0.95	1.00	(a)
prompt S counters	3.9×10^4	0.88	0.93	(b)
$W_{LR} > 0.02$	2.4×10^3	0.76	0.85	(c)
miscellaneous, see text	572	0.71	0.76	(d)
$C(\mathbf{x}) < 25$	160	0.62	0.69	(f)
$|\Delta\theta_{LR}| < 3°$	128	0.61	0.69	

Table 5: Summary of the parameters used in the determination of $BR(\eta \rightarrow \mu^+\mu^-)$.

parameter	value
$N(\eta \rightarrow \mu^+\mu^-)$	114^{+14}_{-15}
$N(pd \rightarrow {}^3He\eta)$	$(1.22 \pm 0.01) \times 10^9$
$\mathcal{A}_{\eta \rightarrow \mu^+\mu^-}$	$(2.91 \pm 0.05) \times 10^{-2}$
$\epsilon^{trigger}_{triple}$	0.92 ± 0.03
$\epsilon^{analysis}_{\mu^+\mu^-}$	0.61 ± 0.05

FIGURE CAPTIONS:

Figure 1: Diagrams for the decay $P^0 \rightarrow \ell^+\ell^-$: (a) QED contribution, (b) weak interaction contribution, (c) hypothetical leptoquark contribution.

Figure 2: Kinematics of pd→^{3}Heη and $\eta \rightarrow \mu^+\mu^-$ with a proton energy 1.6 MeV above threshold. The minimum opening angle of the $\mu^+\mu^-$ pair is 126°.

Figure 3: Top view of the $\eta \rightarrow \mu^+\mu^-$ detection system: LD$_2$ is the liquid deuterium target, M$_L$ and M$_R$ are the left and right muon detectors, Q is the quadrupole magnet, D1 and D2 are dipole magnets, MWPC's are three multi-wire proportional chambers with two sense wire planes each, and hodoscope A and single counter B are plastic scintillators. The dashed lines show the central trajectories for beam protons and for ^{3}He particles from the reaction pd→^{3}Heη.

Figure 4: (a) Distribution of the energy loss in the A hodoscope versus the TOF between A and B. The box shown was used to select the ^{3}He particles. Proton events were eliminated by the high discriminator threshold applied in the readout trigger. (b) Spectrum of the ^{3}He momentum dispersion δ_{He}, after applying the cuts on θ_{He}^h and θ_{He}^v given in Table 2. The distribution contains 15% of the total sample, taken during a 3 day period with stable beam. The result of an event simulation and a second-order polynomial fit to the background are shown as well. The arrows indicate the window chosen to select pd$\rightarrow^3$Heη events; within this region the background amounts to 8%.

Figure 5: Top view of the left muon detector. P, T and S represent the position hodoscopes, trigger hodoscopes and stop counters, respectively. The degraders W and D are made of iron and lead, respectively.

Figure 6: Diagram of the trigger logic. The $P_{L,R}$ and $T_{L,R}$ symbols at the left denote two-fold coincidences between the OR signals of the corresponding horizontal and vertical planes. The L(ook)A(t)M(e) signal, used to interrupt the computer, was the OR of the ^{3}He $(A \cdot \overline{L \cdot R})$ and triple coincidence $(A \cdot L \cdot R)$ data streams. The pulser events (not shown) passed through the triple coincidence logic.

38

Figure 7: Distribution of the time difference between the signals from (a) the two muon detectors and (b) the left detector and the A-plane. The arrows indicate the prompt regions, as defined in the analysis. The distribution in (b) includes only events which are prompt in Δt_{LR}. The prompt peaks are due mainly to the decays $\eta \rightarrow \gamma\gamma$ and $\eta \rightarrow 3\pi^0 \rightarrow 6\gamma$.

Figure 8: Distributions of the opening angle deviation $\Delta\theta_{LR}$, Eq.(6), for various stages in the event selection, as specified in Table 4. Part (e) shows the fraction of (d) with $C(\mathbf{x}) > 25$ and (f) shows the remainder of (d), including the $\eta \rightarrow \mu^+\mu^-$ peak.

Figure 9: The distributions of the event classifier $C(\mathbf{x})$ for (a) signal events with $|\Delta\theta_{LR}| < 3^0$ and (b) background events with $|\Delta\theta_{LR}| > 3.5^0$. Only a small fraction of the background events fall inside the region shown. The arrow shows the cut used to select $\eta \rightarrow \mu^+\mu^-$ candidates. The reduced χ^2 for the comparison between measurement and simulation is 1.7.

Figure 10: Largest energy deposited in any P plane for (a) signal and (b) background. If two overlapping counters were struck, then the average energy deposition was used. The reduced χ^2 for the comparison between measurement and simulation is 1.2.

Figure 11: The product W_{LR} of the range likelihoods on both detectors for (a) signal and (b) background events. The reduced χ^2 for the comparison between measurement and simulation is 1.4.

Figure 12: Distributions of the index of the last hit S plane versus the η emission angle in the horizontal plane, θ_η^h, for measurement and simulation. The straight lines have been fitted to the respective distributions.

Figure 13: Distribution of the opening angle deviation $\Delta\theta_{LR}$ for $C(x) < 25$ (see Fig. 9). The arrows indicate the window used to select $\eta \rightarrow \mu^+\mu^-$ candidates. The reduced χ^2 for the comparison between measurement and simulation is 0.9.

Figure 14: Results of measurements of the branching ratio BR($\eta \rightarrow \mu^+\mu^-$). The statistical and systematic errors have been added in quadrature.

References

[1] L. Arnellos, W.J. Marciano and Z. Parsa, Nucl.Phys. **B196**, 365 (1982).

[2] S.D. Drell, Nuovo Cimento **11**, 693 (1959).

[3] S.M. Berman and D.A. Geffen, Nuovo Cimento **18**, 1192 (1960).

[4] D.A. Geffen and B.-L. Young, Phys.Rev.Lett. **15**, 316 (1965).

[5] L.G. Landsberg, Phys.Rep. **128**, 301 (1985).

[6] V. Barger *et al.*, Phys.Rev.D **25**, 1860 (1982).

[7] K.S. McFarland *et al.*, Phys.Rev.Lett. **71**, 31 (1993).

[8] A. Deshpande *et al.*, Phys.Rev.Lett. **71**, 27 (1993).

[9] J.D. Davies, J.G. Guy, and R.K.P. Zia, Nuovo Cimento **24A**, 324 (1974).

[10] R.I. Dzhelyadin *et al.*, Phys.Lett. **97B**, 471 (1980).

[11] T. Akagi *et al.*, Phys.Rev.Lett. **67**, 2614 (1991).

[12] Particle Data Group, Phys.Rev.D **45**, Part II (1992).

[13] C. Mathiazhagan *et al.*, Phys.Rev.Lett. **63**, 2185 (1989)

[14] T. Akagi *et al.*, Phys.Rev.Lett. **67**, 2618 (1991).

[15] A.P. Heinson *et al.*, Phys.Rev.D **44**, R1 (1991).

[16] D. Wyler, In *Rare Decays of Light Mesons*, ed. B. Mayer, (Editions Frontières, 91192 Gif-sur-Yvette, France, 1990), p. 125.

[17] A.W. Wehman et al., Phys.Rev.Lett. **20**, 748 (1968).

[18] B.D. Hyams et al., Phys.Lett. **29B**, 128 (1969).

[19] J. Berger et al., Phys.Rev.Lett. **61**, 919 (1988).

[20] R.S. Kessler, PhD thesis, University of California, Los Angeles, (1992), unpublished.

[21] R.S. Kessler et al., Phys.Rev.Lett.**70** 892 (1993).

[22] M.Garçon et al., Proc. 7th Lake Louise Winter Inst., ed. B.A. Campbell et al. (World Scientific, Singapore, 1992), p. 337.

[23] F. Plouin et al., Phys.Lett. **B276**, 526 (1992).

[24] B. Bricaud, J.C. Faivre, and J. Pain, IEEE Trans.Nucl.Sci. NS **26**, 4621 (1979).

[25] R. Brun et al., GEANT 3 User's Guide, CERN DD/EE/84-1 (1987).

[26] N.M. Kroll and W. Wada, Phys.Rev. **98**, 1355 (1955).

[27] Ll. Ametller, A. Bramon, and E. Massó, Phys.Rev.D **30**, 251 (1984).

[28] M.J. Savage, M. Luke, and M.B. Wise, Phys.Lett.B **291**, 481 (1992).

(a)   **(b)**   **(c)**

1

Fig. 1

μ^+

p d

$T_P = 893$ MeV

μ^-

$\Theta_\eta < 6^0$

$\Theta_{He} < 1.2^0$
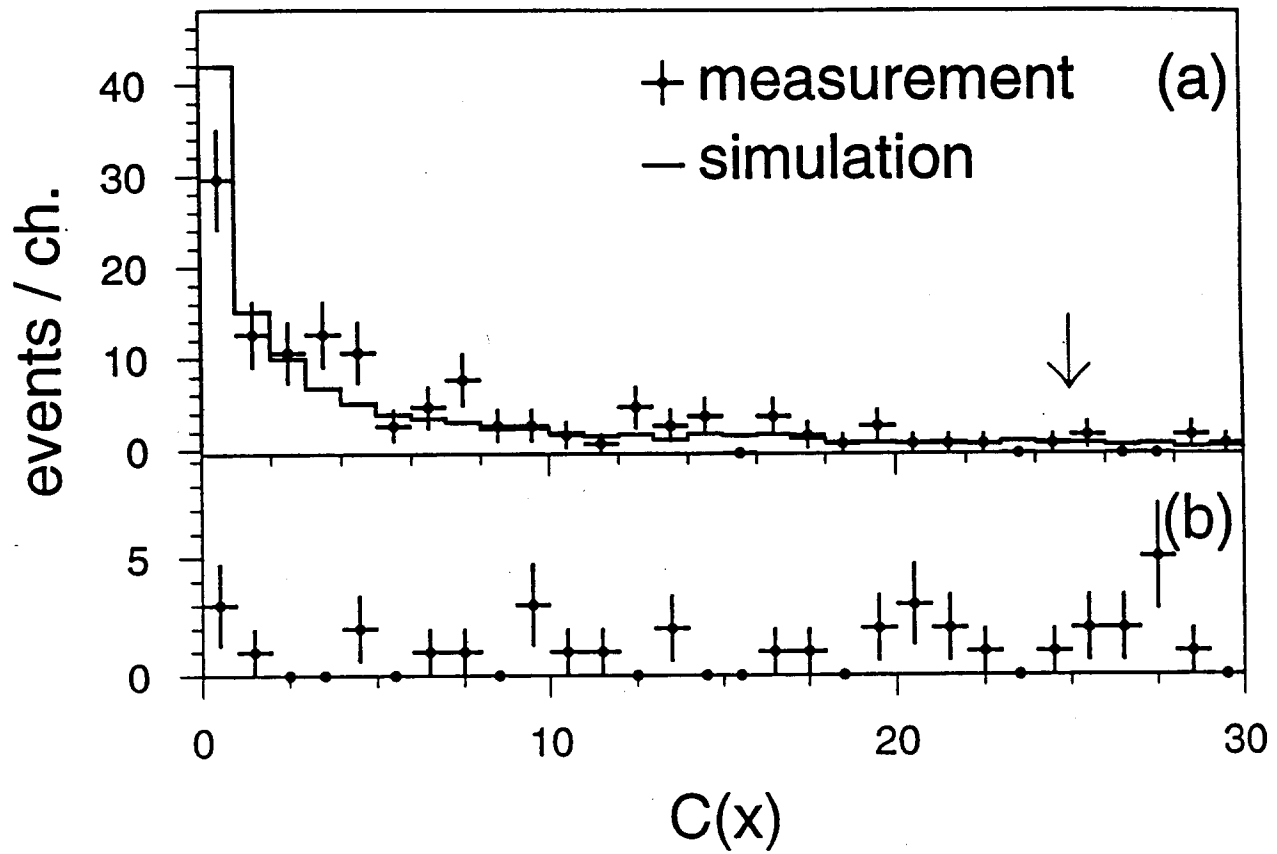
Fig. 2

Fig. 3

Fig. 4

S

T
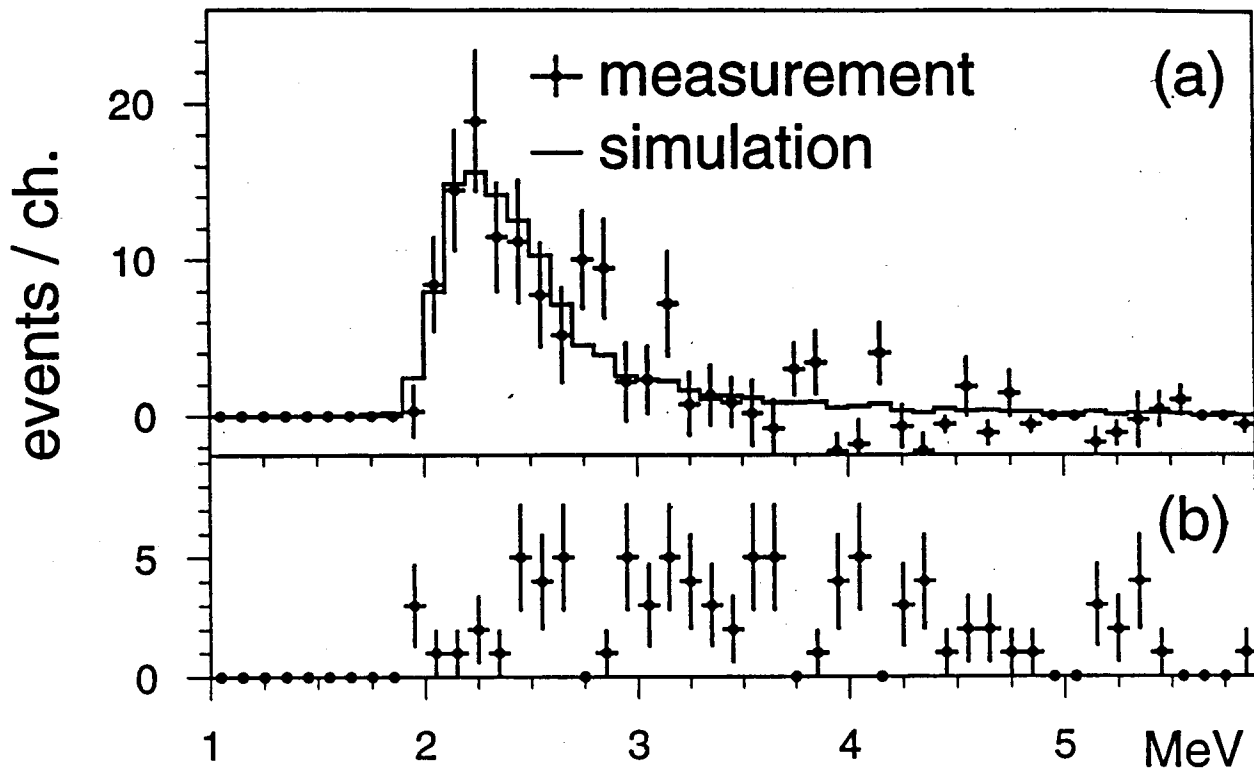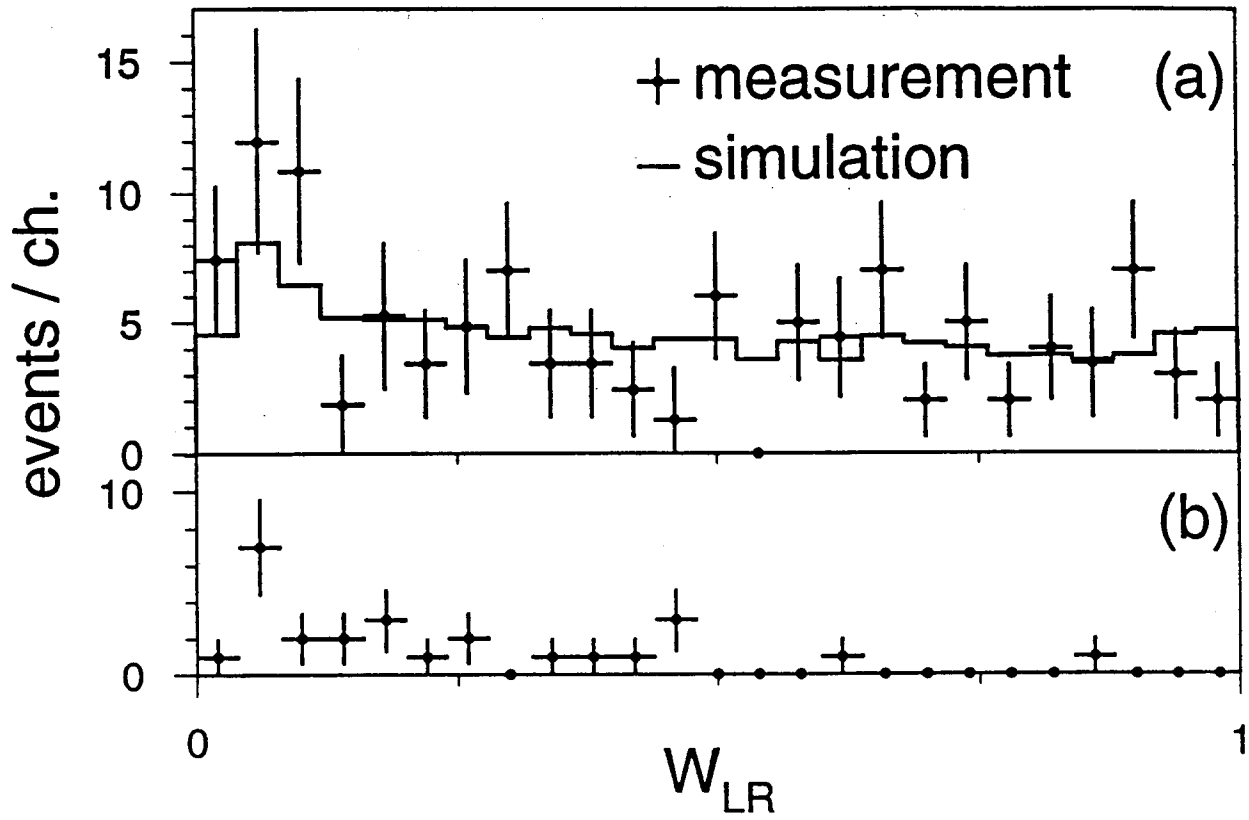
D

P

W

10 cm

Fig. 5

Fig. 6

Fig. 7

Fig. 8
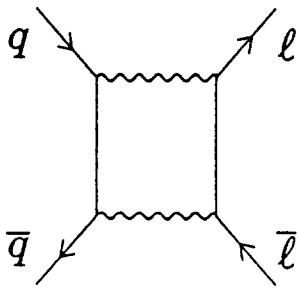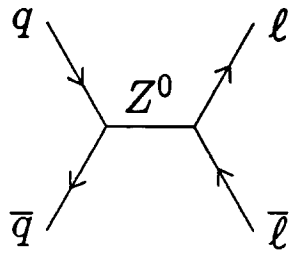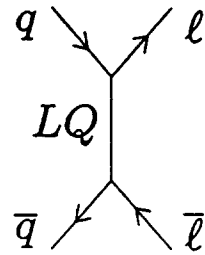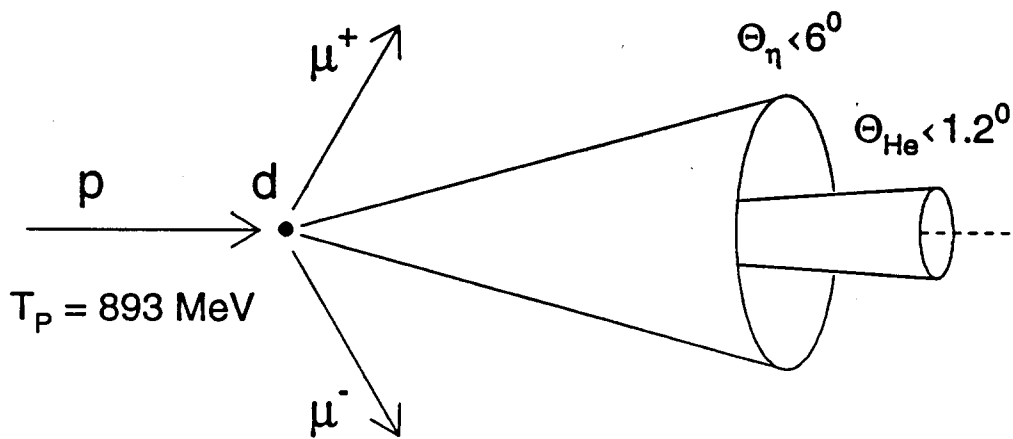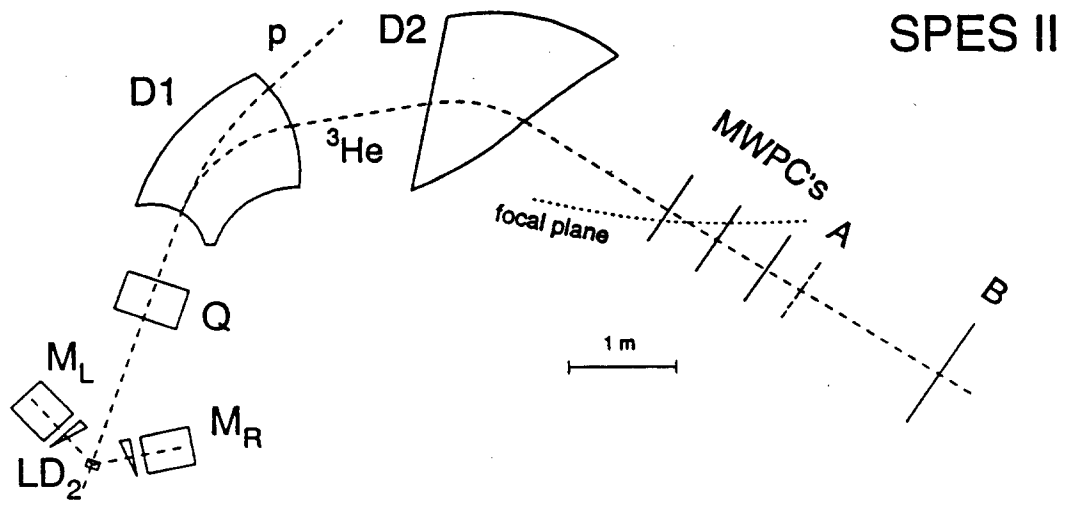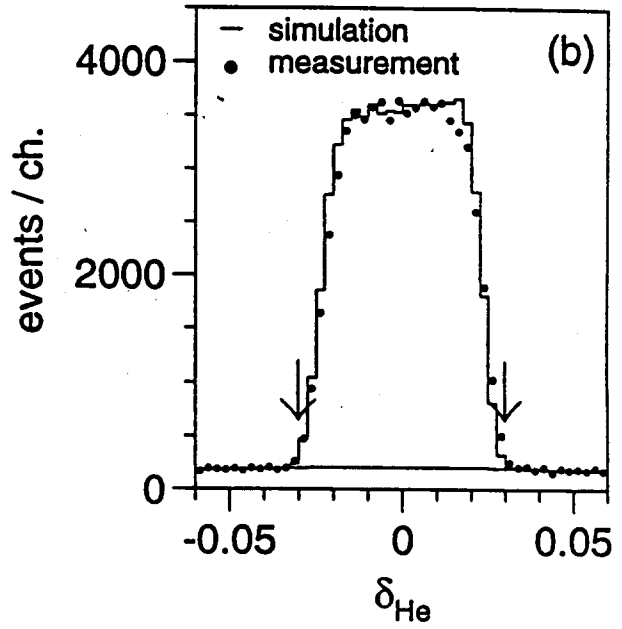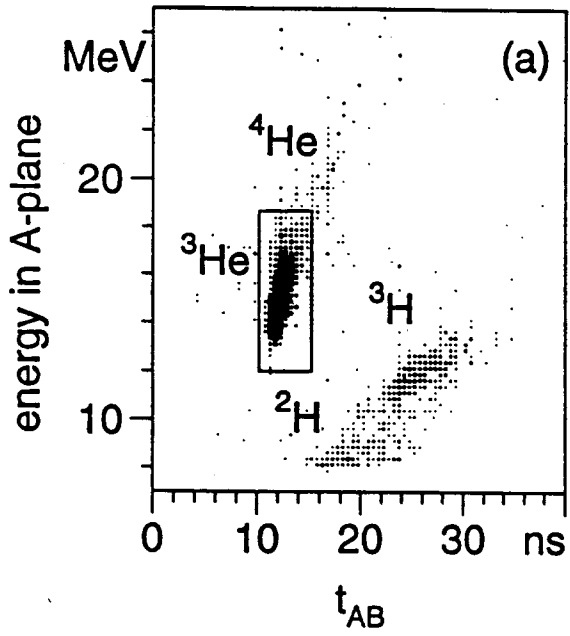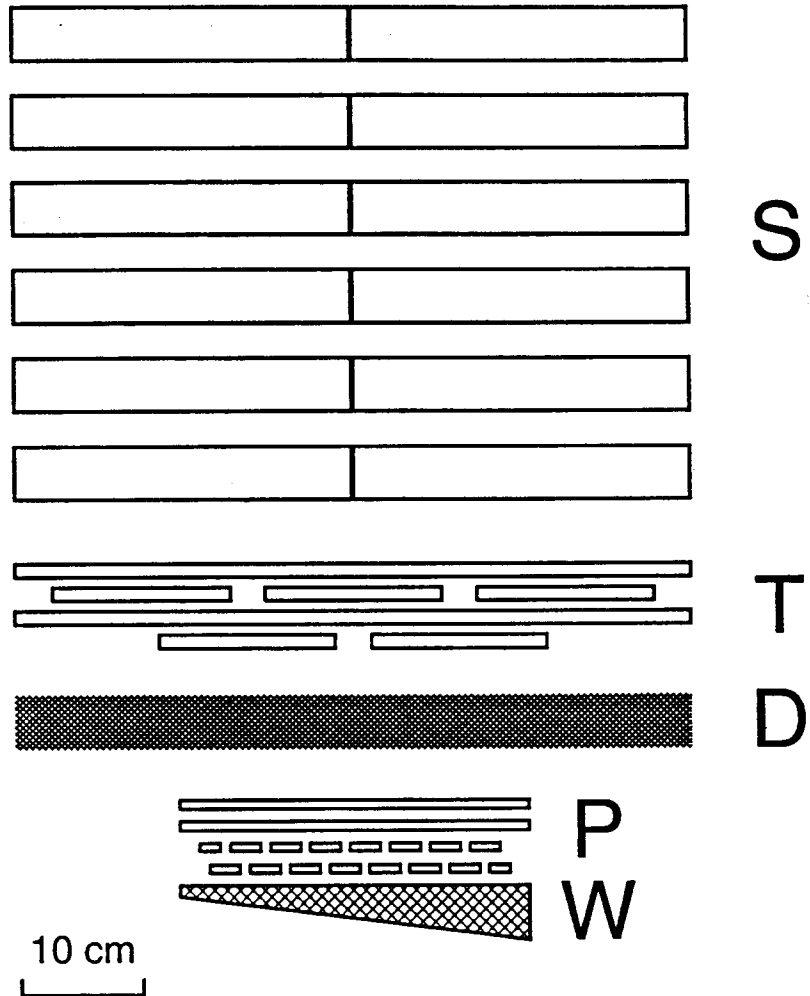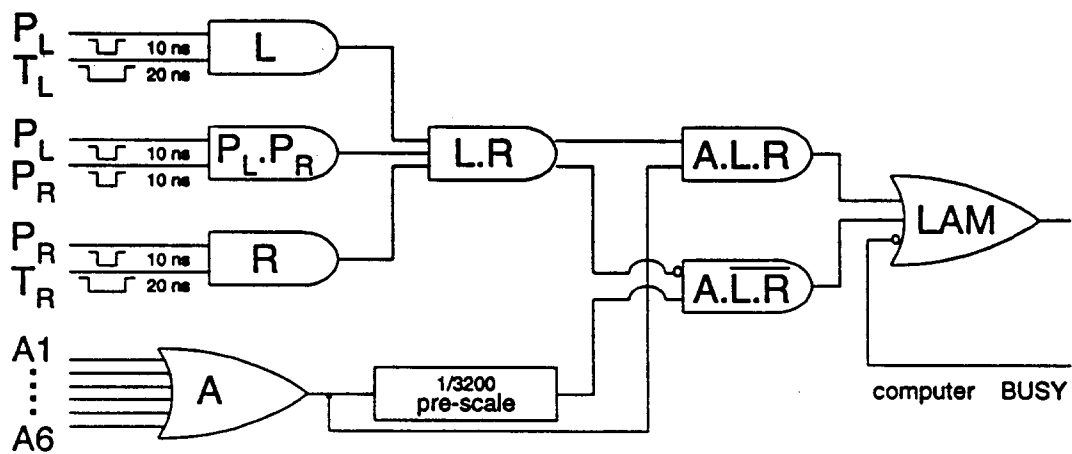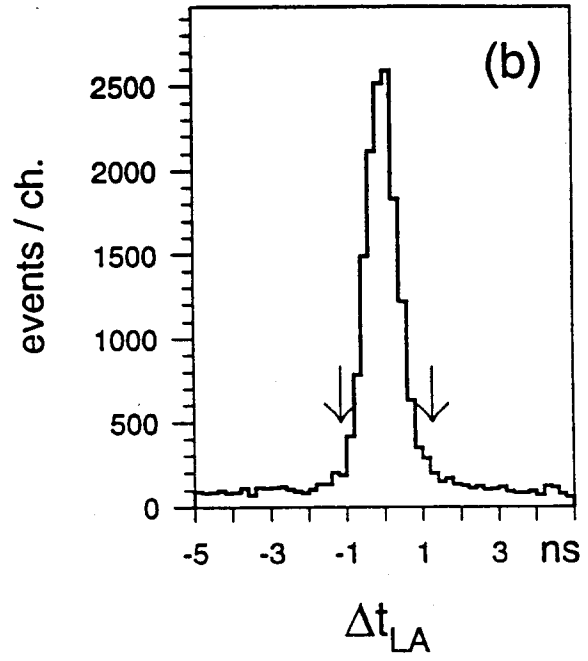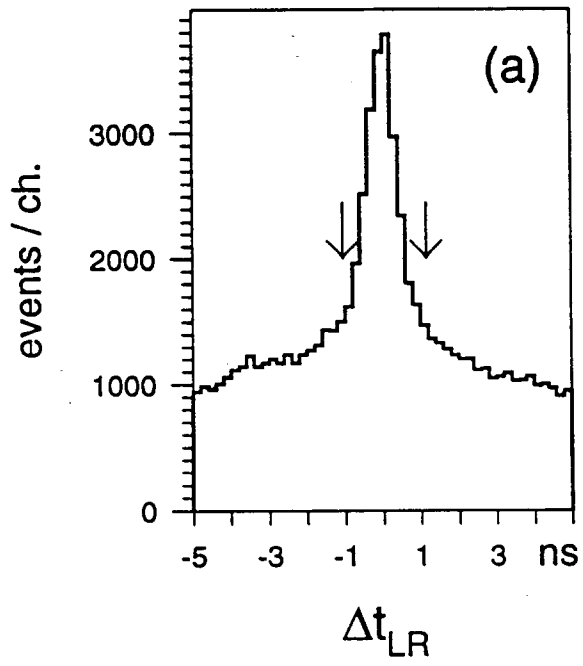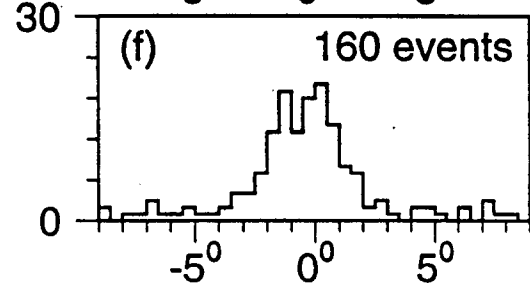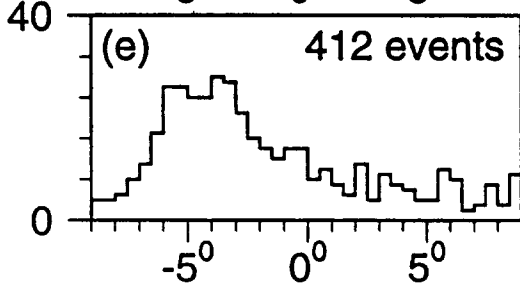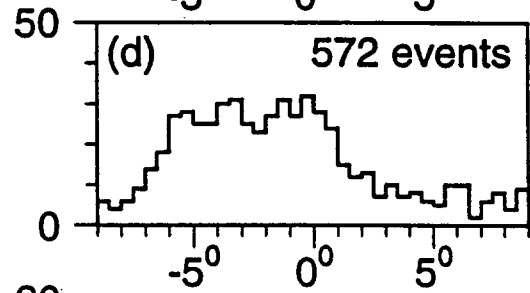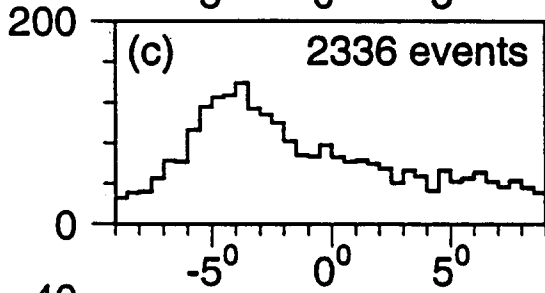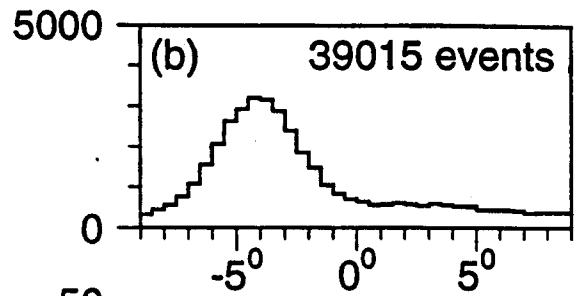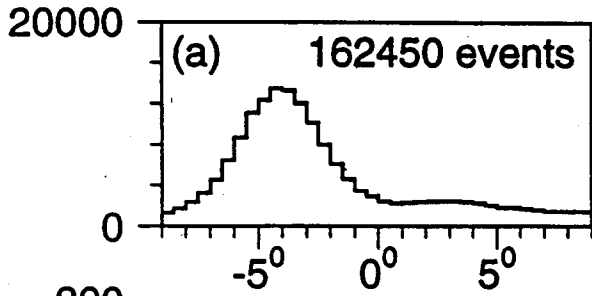
Fig. 9

largest energy in any P plane

Fig. 10

Fig. 11
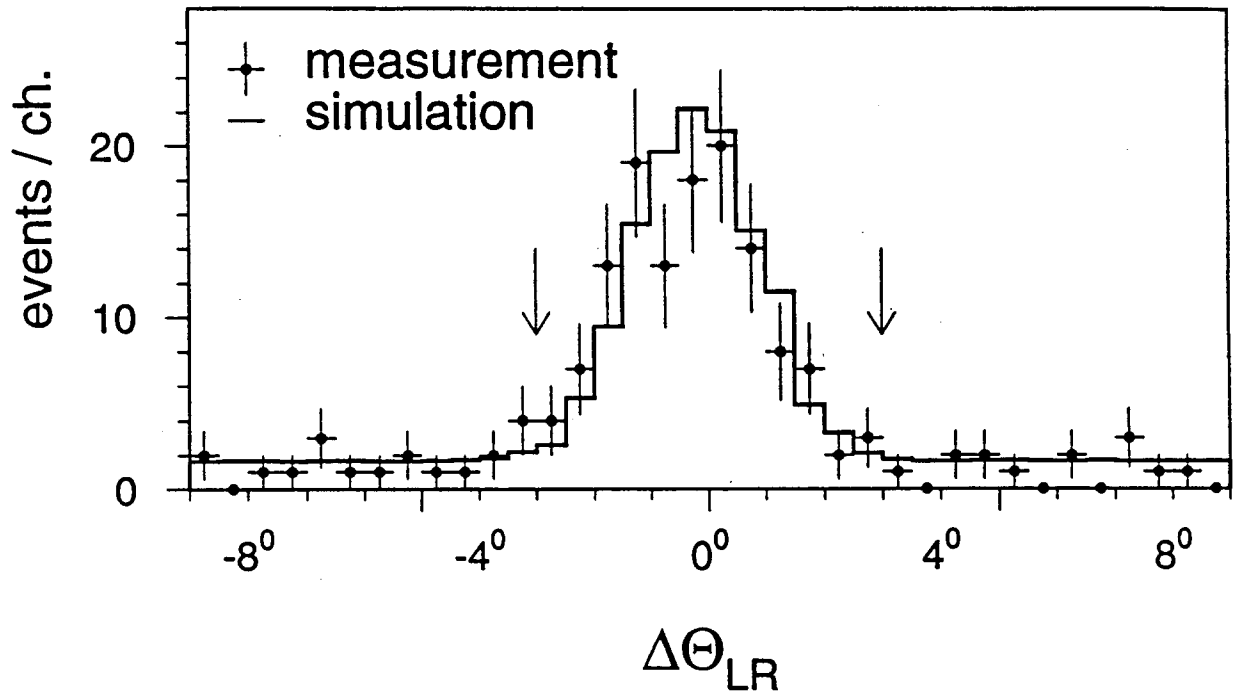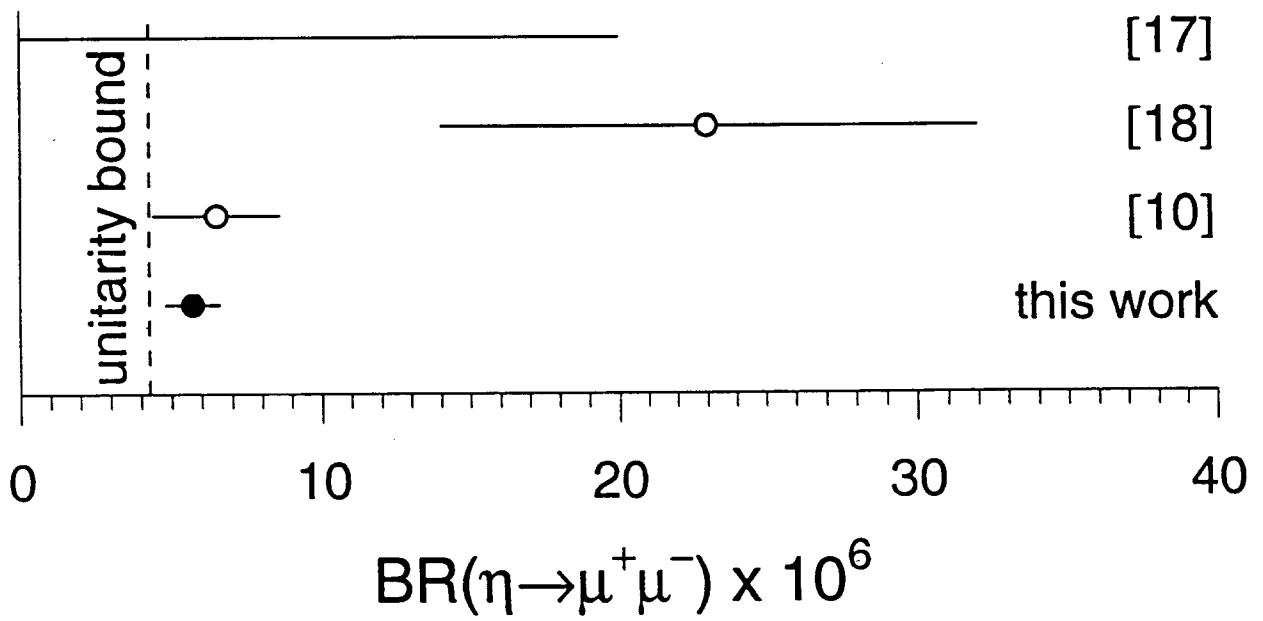
Fig. 12

Fig. 13

$$BR(\eta \rightarrow \mu^+ \mu^-) \times 10^6$$

Fig. 14